Since January 2020 Elsevier has created a COVID-19 resource centre with free information in English and Mandarin on the novel coronavirus COVID-19. The COVID-19 resource centre is hosted on Elsevier Connect, the company's public news and information website.

Journal of Molecular Liquids 325 (2021) 114765

Contents lists available at ScienceDirect

Journal of Molecular Liquids

journal homepage: www.elsevier.com/locate/molliq

Structural investigations, quantum mechanical studies on proton and metal affinity and biological activity predictions of selpercatinib

Nabil Al-Zaqri [a,b], T. Pooventhiran [c], Fahad A. Alharthi [a], Utsab Bhattacharyya [c], Renjith Thomas [c,*]

[a] Department of Chemistry, College of Science, King Saud University, P.O. Box 2455, Riyadh 11451, Saudi Arabia
[b] Department of Chemistry, College of Science, Ibb University, P. O. Box 70270, Ibb, Yemen
[c] Department of Chemistry, St. Berchmans College (Autonomous), Changanassery, Kerala, India

ARTICLE INFO

Article history:
Received 17 August 2020
Received in revised form 23 October 2020
Accepted 10 November 2020
Available online 13 November 2020

Keywords:
DFT
ELF
Selpercatinib
Docking
Proton affinity

ABSTRACT

Cancer of the lungs and thyroid is particularly difficult to manage and treat. Notably, selpercatinib has recently been suggested as an effective drug to combat these diseases. The entire world is currently tackling the pandemic caused by the SARS-CoV-19 virus. Numerous pharmaceuticals have been evaluated for the management of the disease caused by SARS-CoV-19 (i.e., COVID-19). In this study, selpercatinib was proposed as a potential inhibitor of different SARS-CoV-19 proteins. Several intriguing effects of the molecule were found during the conducted computational investigations. Selpercatinib could effectively act as a proton sponge and exhibited high proton affinity in solution. Moreover, it was able to form complexes with metal ions in aqueous solutions. Specifically, the compound displayed high affinity towards zinc ions, which are important for the prevention of virus multiplication inside human cells. However, due to their charge, zinc ions are not able to pass the lipid bilayer and enter the cell. Thus, it was determined that selpercatinib could act as an ionophore, effectively transporting active zinc ions into cells. Furthermore, various quantum mechanical analyses, including energy studies, evaluation of the reactivity parameters, examination of the electron localisation and delocalisation properties, as well as assessment of the nonlinear optical (NLO) properties and information entropy, were conducted herein. The performed docking studies (docking scores −9.3169, −9.1002, −8.1853 and −8.1222 kcal mol^{-1}) demonstrated that selpercatinib strongly bound with four isolated SARS-CoV-2 proteins.

1. Introduction

Cancer remains the world's leading cause of death [1]. One main reasons for human T-cell lymphoma is the mutation of an oncogene in the NIH-3 T3 cells [2]. Selpercatinib is a rearranged during transfection (RET)-specific tyrosine kinase inhibitor (TKI) and has been shown as an effective agent for the treatment of the disease [3]. About 10% of thyroid cancers originate in the parafollicular C cells of the thyroid, which produce the calcitonin hormone. Gene mutation and the resulting medullary thyroid cancer lead to increased levels of calcitonin [4]. Alcetinib was developed as an agent for the treatment of cancers associated with RET mutations [5]. It is noteworthy that the Food and Drug Administration (FDA) in the USA recently approved the use of selpercatinib, also known as Retevmo, for the management of three types of cancers caused by RET mutations.

Recently, a new strain of coronavirus, namely SARS-CoV-2, has posed a threat to the human health worldwide [6]. The rapid spread of the virus has led to classification of the outbreak as a pandemic [7]. Numerous research groups all over the world are working on the development of a vaccine or medicine to prevent or treat COVID-19, which is the disease caused by SARS-CoV-2. At the time of writing this article, COVID-19 resulted in 600,000 deaths globally. Hence, scientists are determined to establish the pathology [8] and epidemiology [8] of the disease as well as to develop medicines and vaccines against it [9]. As the development of new cures is a challenging process, a number of existing drugs have been proposed for the management of COVID-19 [10]. For instance, despite contrasting results, chloroquine was highlighted as an effective medicine for the managements of the disease; however, it is now discontinued [11]. At present, remdesivir is widely used for the treatment of pneumonia associated with COVID-19 [12]. Lopinavir, umifenovir, favipiravir and oseltamivir have also been demonstrated as potentially active compounds against the virus [10]. Because the design and development of drugs is a time consuming process, studies on utilising existing agents for the management and treatment of COVID-19 are important. In the present study, we investigated selpercatinib as a potential anti-SARS-CoV-2 drug candidate.

In this work, we evaluated the structural and electronic features of selpercatinib. Computational chemistry is a powerful tool for studying the behaviours of various molecules and materials [13–17]. Hence, in the current study, we examined the geometry, electronic properties and reactivity descriptors of selpercatinib using density functional

* Corresponding author.
E-mail address: renjith@sbcollege.ac.in (R. Thomas).

https://doi.org/10.1016/j.molliq.2020.114765
0167-7322/

theory (DFT) calculations. We also analysed the intramolecular electron delocalisations, non-covalent interactions and average local ionisation energy indices of the compound. The data was supplemented by NICS calculations. Moreover, the proton affinity of selpercatinib in solution was evaluated using theoretical calculations. Intriguingly, high proton and metal affinities were determined. The affinity of the agent towards zinc was also investigated. It was found that zinc ions could inhibit the multiplication of the virus inside host cells. Hence, it was hypothesised that if selpercatinib could act as an ionophore, enabling the diffusion of the metal ions into cells through the lipid bilayer, it could effectively control further spread of the virus. The most important aspect of the study was the potential use of the drug as a supplementary medicine for the management of COVID-19 caused by SARS-CoV-19. Hence, we also performed molecular docking of the compound with four known SARS-CoV-19 proteins.

2. Methods

The selpercatinib molecule was optimised using the Gaussian-09 software [18]. The DFT-B3LYP method [19,20] and 6-311G+ (2d,p) basis set were employed for the optimisation [21,22]. To ensure the lack of imaginary frequency, frequency calculations were performed to confirm that the obtained geometry corresponded to a global minimum of the optimised geometry. The same geometry was used for the analysis of the frontier molecular orbitals (FMO) and natural bond orbitals (NBO) as well as for nonlinear optical (NLO) studies. For the simulation of the ultraviolet (UV)-visible spectrum, time-dependent density functional theory (TD-DFT) analysis with long-range corrected CAM-B3LYP functional [23,24] and 6-311G+ (2d,p) basis set was conducted using GaussSum to establish whether the electronic transitions were time-dependent phenomena [25]. Selpercatinib contains more than two possible reaction sites, e.g. methoxy, methylpyridine, 3,6-diazobicycloheptane, pyridine, carbonitrile and pyrazolopyridine groups. The total electrostatic potential, average localised ionisation energy, electron localisation functions, localised orbital locators, reduced density gradients, localised entropy interactions and non-covalent interactions of selpercatinib were calculated using the Multiwavefunction software [26]. The biological activity of the compound against SARS-CoV-2 was evaluated by downloading the structures of the viral proteins from the Protein Data Bank (PDB) at the RCSB website [27]. The energy values were obtained from SwissDock [28,29], while the score values were acquired from PatchDock [30,31]. The docked results were collected from the bio-discovery studio software.

3. Results

3.1. Molecular geometry of selpercatinib

The molecular structure of selpercatinib was optimised by DFT using the DFT-B3LYP method and 6-311G+ (2d,p) basis set. The optimised structure of the compound is illustrated in Fig. 1. As it can be seen, selpercatinib contains a number of rings and functional groups, including methylpyridine, 3,6-diazobicycloheptane, pyridine, carbonitrile and pyrazolopyridine moieties.

A summary of the calculated physical parameters for selpercatinib is shown in Table 1. The bond angles for 26C–1O–33C, 21C–7 N–26C, 1O–26C–7 N, 4 N–16C–18C, 11C–4 N–12C, 11C–13C–12C, 14C–5 N–15C, 15C–5 N–17C, 14C–5 N–17C, 5 N–17C–6 N, 17C–6 N–23C, 28C–8 N–32C, 9 N–8 N–28C, 8 N–9 N–34C, 30C–2O–36C, 2O–36C–35C, 36C–35C–38C, 3O–35C–36C, 35C–3O–70H and 3O–35C–37C were determined at 117.36°, 117.91°, 119.76°, 111.98°, 85.55°, 82.99°, 120.00°, 119.14°, 120.35°, 116.81°, 118.73°, 124.53°, 113.30°, 104.58°, 117.99°, 108.88°, 111.21°, 101.86°, 108.68° and 110.31°, respectively. In addition, the bond lengths for 1O-26C, 1O-33C, 7 N–21C, 7 N–26C, 16C-18C, 4 N–16C, 4 N–11C and 4 N–12C were established at 1.35, 1.43, 1.34, 1.32, 1.51, 1.46, 1.51 and 1.51 Å, respectively.

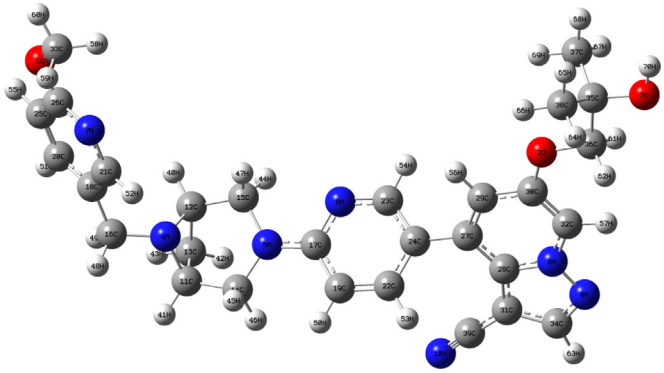

Fig. 1. Molecular structure of selpercatinib.

3.2. FMO analysis

FMO theory provides valuable information on the energy band gap. Based on the energies of the highest occupied molecular orbital (HOMO) and lowest unoccupied molecular orbital (LUMO), various physical and chemical descriptors of a molecule can be predicted, enabling evaluation of its reactivity, stability and biological activity [32]. In this study, the HOMO and LUMO energies were calculated using the B3LYP/6–311 + G(2d,p) basis set. The frontier energies and the related chemical descriptors are summarised in Table 2 [33,34].

The HOMO, LUMO and energy gap (ΔE) of selpercatinib were determined at −5.58, −1.69 and 3.90 eV, respectively. The other evaluated chemical descriptors included ionisation energy (I), electron affinity (A), global hardness (η), global softness (S), chemical potential (μ), electronegativity (χ), electrophilicity index (ω) [35] and nucleophilicity index (N) [36]. The values of these descriptors were established at 5.58, 1.69, 1.95, 0.51, −3.64, 3.64, 3.39 and 0.29, respectively. The energy gap between the HOMO and LUMO was only 3.90 eV, indicating that the

Table 1
Calculated physical parameters for selpercatinib.

Bond length	Å	Bond Angle	Value (in ^{0})
R(1,26)	1.35	A(26,1,33)	117.36
R(1,33)	1.43	A(21,7,26)	117.91
R(7,21)	1.34	A(1,26,7)	119.76
R(7,26)	1.32	A(4,16,18)	111.98
R(16,18)	1.51	A(11,4,12)	85.55
R(4,16)	1.46	A(11,13,12)	82.99
R(4,11)	1.51	A(14,5,15)	120.00
R(4,12)	1.51	A(15,5,17)	119.14
R(11,14)	1.52	A(14,5,17)	120.35
R(11,13)	1.54	A(5,17,6)	116.81
R(12,13)	1.55	A(17,6,23)	118.73
R(12,15)	1.52	A(28,8,32)	124.53
R(5,14)	1.46	A(9,8,28)	113.30
R(5,15)	1.47	A(8,9,34)	104.58
R(5,17)	1.37	A(30,2,36)	117.99
R(6,17)	1.35	A(2,36,35)	108.88
R(17,19)	1.42	A(36,35,38)	111.21
R(24,27)	1.48	A(3,35,36)	101.86
R(8,28)	1.38	A(35,3,70)	108.68
R(8,9)	1.36		
R(8,32)	1.37		
R(9,34)	1.33		
R(31,39)	1.41		
R(10,39)	1.16		
R(28,31)	1.41		
R(2,30)	1.36		
R(2,36)	1.43		
R(35,36)	1.53		
R(35,37)	1.53		
R(35,38)	1.53		
R(3,35)	1.44		
R(3,70)	0.96		

Table 2
FMO properties of selpercatinib.

HOMO	−5.58
LUMO	−1.69
Energy gap ΔE	3.90
Ionisation energy (I = εHOMO = −HOMO)	5.58
Electron affinity (A = εLUMO = −LUMO)	1.69
Global hardness (η = (I − A)/2)	1.95
Global softness (S = 1/η)	0.51
Chemical potential (μ = −(I + A)/2)	−3.64
Electronegativity (χ = −μ)	3.64
Electrophilicity index (ω = μ2/2η	3.39
Nucleophilicity index (*N* = 1/ω)	0.29
ΔNmax	1.87
Electroaccepting power ω + = A2/2(I − A)	0.37
Electrodonating power ω + = I2/2(I − A)	−59.98

electron transition in this compound is not difficult [33]. Chemical hardness refers [37] to the ability of a compound to resist deformation while, polarizability or softness [38] is the inverse measure of resistance to deformation and hence inversely related to hardness [39]. A more detailed discussion of reactivity is provided in the subsequent sections.

3.3. TD-DFT study

As time-dependent phenomena, electronic transitions, and consequently electronic spectra, cannot be modelled by DFT simulations. TD-DFT simulations, which employ Tamm–Dancoff approximations must be used instead [40–44]. In this work, TD-DFT simulations with the CAM-B3LYP functional and 6-311G+ (2d,p) basis set were conducted using the integral equation formalism (IEFPCM) solvation model and methanol as the solvent [45–48]. Fig. 2 illustrates the simulated UV–visible spectrum of selpercatinib. The major peak with an oscillating strength of 0.46 was detected at 307.1 nm. The two major contributions for this transition were from HOMO to LUMO (84%) and from HOMO−1 to LUMO (11%). Notably, **Fig. S1** demonstrating the FMO indicates that HOMO, HOMO-1 and LUMO are located in the similar region of the molecule. Furthermore, the second transition was observed at 273.19 nm with an oscillating strength of 0.10. Thus, the second transition was less intense than the first. In this case, the major contributions were from HOMO−1 to LUMO (42%) and from HOMO to LUMO+2 (25%). The density of states (DOS) spectrum (Fig. 3) showed that the band gaps near the HOMO and LUMO as well as the frontier orbitals were free from core electron overlaps.

3.4. NLO properties of selpercatinib

Evaluation of light–matter interactions is remarkably important, particularly in the case of organic molecules. The ability of a molecule to bend linear light can be determined by the analysis of the polarisability and hyperpolarisability values obtained from Raman spectrum simulations. Consideration of the NLO activity is especially significant for application of organic compounds in the electronics industry [49–52]. Simulations are typically conducted on the same theoretical level as that used for the optimisation studies and the results are compared with standard NLO active substances such as urea and *p*-nitroacetanilide [53–55]. The NLO properties of selpercatinib as well as their comparison with the characteristics of urea and *p*-nitroacetanilide are shown in Table 3.

Selpercatinib exhibits a dipole moment (μ) of 2.9799 D, which is 0.9950 times greater than that of urea and 3.6106 times greater than that of *p*-nitroacetanilide. Morever, hyperpolarisability (β) of the studied compound was established at $3714.3349^{*}10^{-37}$ esu, which is 42.0605 times greater than that of urea and 4.6058 times greater than that of *p*-nitroacetanilide. The mean polarisability (α_0) of selpercatinib is $424.0073^{*}10^{-23}$ esu; hence, it is 17.4480 times higher than that of urea and 3.4511 times higher than that of *p*-nitroacetanilide. Furthermore, the anisotropy of the polarisability (Δα) of the molecule was determined at $950.3143^{*}10^{-23}$ esu, which is 17.9165 times greater than that of urea and 2.7533 times greater than that of *p*-nitroacetanilide. Lastly, the molar refractivity (MR) of selpercatinib was established at 10699.84444 esu; therefore, it is 17.448 times higher than that of urea and 3.4512 times higher than that of *p*-nitroacetanilide.

3.5. Study of NBO of selpercatinib

Intramolecular electron displacements are remarkably important as they determine the inherent stability of a compound. Analysis of NBO can be used to evaluate interactions by hyperconjugation [51–53]. The

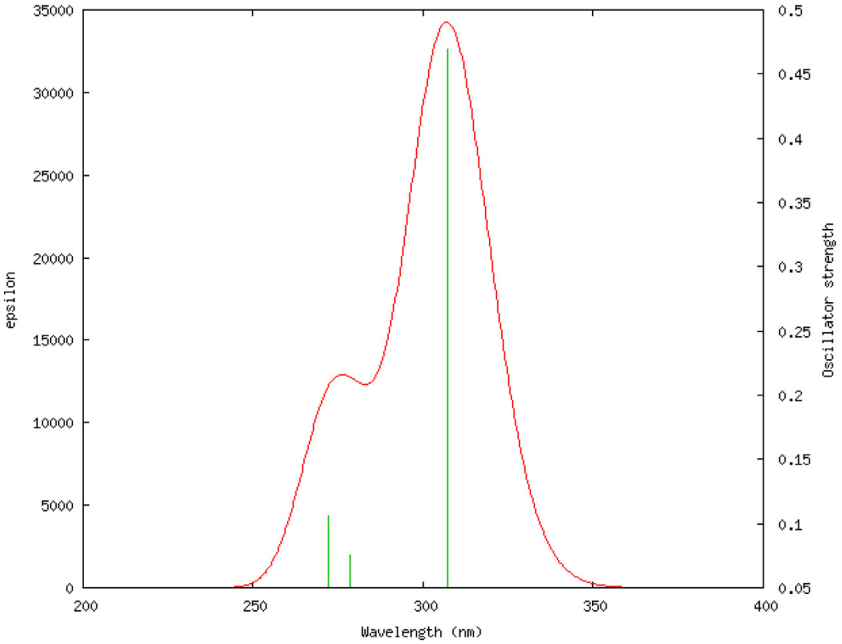

Fig. 2. UV–visible spectrum of selpercatinib simulated by TD-DFT CAM-B3LYP/6-311G+ (2d,p) in methanol using the IEFPCM implicit solvation model.

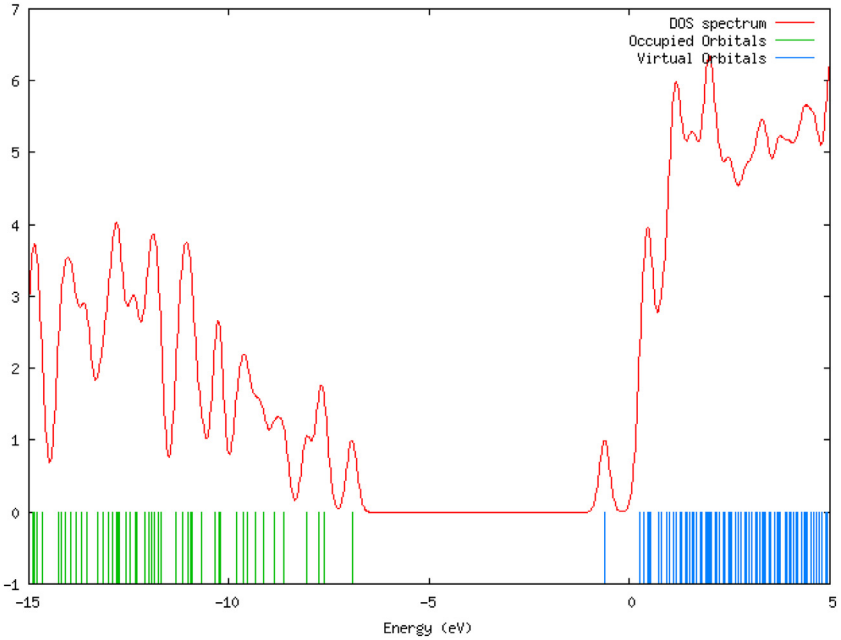

Fig. 3. DOS spectrum indicating the occupied and virtual orbitals of selpercatinib with a distinct energy gap.

occupancy values of NBOs and their delocalisation energies provide useful information about the above-mentioned stabilisations [56–58]. In this study, the NBO calculations were conducted using the NBO suite available within the Gaussian 09 software [59].

Table 4 shows the occupancy data of NBOs of selpercatinib. Electron transitions can occur from the donor bonding orbitals to the acceptor lone pair, anti-bonding and anti-Rydberg orbitals exhibiting the corresponding occupancies with suitable energies. In this work, we predominantly focused on the most significant transitions. It was established that the electrons in the σ (O3–C35) orbital with an occupancy of 1.99 transitioned to R* (O3) with a delocalisation energy of 4329.48 kcal mol^{-1}. Moreover, the electrons in σ (O3–H70) with an occupancy of 1.99 transitioned to R* (O3) with an energy of 6329.79 kcal mol^{-1}. The occupancy of σ (C16–H49) was determined at 1.99. The electrons in this orbital transitioned to R* (O3) with a delocalisation energy of 5312.21 kcal mol^{-1}. In the case of σ (C17–C19) with an occupancy of 1.98, the electrons transitioned to R* (O3) with a delocalisation energy 6850.61 kcal mol^{-1}. In addition, the electrons in the σ (C18–C20) orbital, which displayed an occupancy of 1.98, transitioned to R* (O3) with an energy of 10,167.24 kcal mol^{-1}. The electrons in the σ (C19–C22) orbital with occupancy of 1.98 transitioned to R* (O3) with an energy of 16,534.65 kcal mol^{-1}. The electrons from σ (C19–H50), which exhibited occupancy of 1.98 transitioned to R* (O3) with a delocalisation energy of 20,864.88 kcal mol^{-1}. Lastly, the electrons from the σ (C20–C25) orbital with an occupancy of 1.98 transitioned to R* (O3) with an energy of 20,135.46 kcal mol^{-1}.

It is known that electrons transitions can also occur from the donor core pair orbitals to the acceptor anti-bonding and anti-Rydberg orbitals exhibiting the corresponding occupancies with suitable energies. In the case of selpercatinib, the electrons transitioned from CR (O3) with an occupancy of 1.99 to R* (O3) with an energy of 2735.82 kcal mol^{-1}. In addition, electron transitions can occur from the donor lone pair orbital to the acceptor anti-Rydberg orbitals displaying the corresponding occupancies with suitable energies. In the studied case, these type of transitions were determined from n (O3) with an occupancy of 1.96 to R* (O3), R* (C30), R* (C31), R* (C32), R* (C33), R* (C35), R* (C36) and R* (C39) with energies of 2559.65, 130.38, 201.55, 248.72, 225.82, 450.30, 430.81 and 1044.68 kcal mol^{-1}, respectively.

Furthermore, electron transitions can take place from the donor anti-bonding orbitals to the acceptor anti-bonding orbitals exhibiting the corresponding occupancies with suitable energies. It was established that electron transitions occurred from σ* (C28–C31) and σ* (C30–C32) with occupancies of 0.55 and 0.32 to σ* (C27–C29) and σ* (C27–C29) exhibiting energies of 157.92 and 128.04 kcal mol^{-1}, respectively. Electrons also transitioned from the σ* (N7–C17) orbital with occupancy of 0.48 to σ* (C19–C22) and σ* (C23–C24) with energies of 117.19 and 141.14 kcal mol^{-1}, correspondingly. Lastly, the electrons from the σ* (N7–C26) orbital with occupancy of 0.44 transitioned

Table 3
NLO properties of selpercatinib.

Non-linear property	selpercatinib	urea	*p*-nitroacetanilide	Comparison of selpercatinib with urea and *p*-nitroacetanilide
Dipole moment (μ)	2.9799 D	2.9946 D	0.8253 D	0.9950 times greater than urea and 3.6106 times greater than *p*-nitroacetanilide
Hyperpolarisability (β)	$3714.3349*10^{-37}$ esu	$88.3092*10^{-37}$ esu	$806.4447*10^{-37}$ esu	42.0605 times greater than urea and 4.6058 times greater than *p*-nitroacetanilide
Mean polarisability (α_0)	$424.0073*10^{-23}$ esu	$24.3006*10^{-23}$ esu	$122.8583*10^{-23}$ esu	17.4480 times greater than urea and 3.4511 times greater than *p*-nitroacetanilide
Anisotropy of polarisability (Δα)	$950.3143*10^{-23}$ esu	$53.0411*10^{-23}$ esu	$345.1504*10^{-23}$ esu	17.9165 times greater than urea and 2.7533 times greater than *p*-nitroacetanilide
Molar refractivity (MR)	10,699.84444 esu	613.2114 esu	3100.2575 esu	17.448 times greater than urea and 3.4512 times greater than *p*-nitroacetanilide

Table 4
The occupancy data of natural bond orbitals (NBO) of selpercatinib.

Donor NBO (i)	Acceptor NBO (j)	E(2) kcal mol^{-1}	E(j)-E(i) a.u.	F(i,j) a.u.	Occupancy
BD (1) C 16 - H 49	RY* (3) C 31	474.36	2.39	0.952	1.99
BD (1) C 17 - C 19	RY* (12) C 38	8687.41	2.32	4.027	1.98
BD (1) C 17 - C 19	RY* (2) C 39	7952.29	2.05	3.624	1.98
BD (1) C 17 - C 19	RY* (12) O 3	6850.61	2.53	3.736	1.98
BD (1) C 17 - C 19	RY* (10) C 35	793.97	4.39	1.675	1.98
BD (1) C 17 - C 19	RY* (12) C 32	643.21	4.8	1.578	1.98
BD (1) C 17 - C 19	RY* (10) C 33	595.82	4.85	1.526	1.98
BD (1) C 17 - C 19	RY* (3) C 31	594.26	4.99	1.545	1.98
BD (1) C 18 - C 20	RY* (10) O 3	10,167.2	0.18	1.213	1.98
BD (1) C 18 - C 20	RY* (5) C 39	769.77	0.96	0.771	1.98
BD (1) C 18 - C 20	RY* (11) C 36	492.87	1.39	0.744	1.98
BD (1) C 18 - C 20	RY* (10) C 35	474.39	1.06	0.636	1.98
BD (1) C 19 - C 22	RY* (10) O 3	16,534.7	0.09	1.101	1.98
BD (1) C 19 - C 22	RY* (5) C 39	696.83	0.87	0.699	1.98
BD (1) C 19 - H 50	RY* (12) O 3	20,864.9	0.42	2.645	1.98
BD (1) C 19 - H 50	RY* (9) C 36	7610.47	0.78	2.189	1.98
BD (1) C 19 - H 50	RY* (5) C 39	1181.71	2.18	1.44	1.98
BD (1) C 19 - H 50	RY* (10) C 35	767.61	2.28	1.186	1.98
BD (1) C 19 - H 50	RY* (12) C 32	576	2.69	1.118	1.98
BD (1) C 19 - H 50	RY* (10) C 33	529.12	2.74	1.081	1.98
BD (1) C 19 - H 50	RY* (3) C 31	517.35	2.87	1.094	1.98
BD (1) C 20 - C 25	RY* (6) O 3	20,135.5	5.04	9.044	1.98
BD (1) C 20 - C 25	RY* (1) H 70	10,354.6	6.92	7.598	1.98
BD (1) C 20 - C 25	BD* (1) C 38 - H 66	8695.02	7.27	7.124	1.98
BD (1) C 20 - C 25	RY* (12) C 36	7967.61	7.54	6.959	1.98
BD (1) C 20 - C 25	RY* (12) C 38	6041.7	9.24	6.708	1.98
BD (1) C 20 - C 25	RY* (2) C 39	5043.42	8.98	6.036	1.98
BD (1) C 20 - C 25	RY* (10) C 35	854.43	11.31	2.791	1.98
BD (1) C 20 - C 25	RY* (12) C 32	732.2	11.73	2.631	1.98
BD (1) C 20 - C 25	RY* (3) C 31	690.91	11.91	2.574	1.98
BD (1) C 20 - C 25	RY* (10) C 33	681.07	11.77	2.542	1.98
BD (1) C 20 - C 25	RY* (14) C 37	668.01	14.8	2.823	1.98
BD (1) C 20 - C 25	RY* (13) C 30	549.02	12.14	2.318	1.98
BD (1) C 23 - H 54	RY* (4) O 3	504.63	0.1	0.202	1.98
BD (1) O 3 - C 35	RY* (5) C 39	912.99	0.57	0.648	1.99
BD (1) O 3 - C 35	RY* (11) C 36	482.78	1.01	0.624	1.99
BD (1) O 3 - H 70	RY* (4) O 3	6329.79	0.17	0.942	1.99
BD (1) O 3 - H 70	RY* (5) C 39	2379.46	0.33	0.787	1.99
BD (1) O 3 - H 70	RY* (10) C 35	969.05	0.42	0.574	1.99
BD (1) O 3 - H 70	RY* (11) C 36	967.18	0.76	0.767	1.99
BD (1) O 3 - H 70	RY* (12) C 32	535.17	0.84	0.601	1.99
BD (1) O 3 - H 70	RY* (10) C 33	492.22	0.89	0.591	1.99
BD (1) O 3-C 35	RY* (7) O 3	4329.48	0.22	0.88	1.99
CR (1) O 3	RY* (6) O 3	2735.82	12.49	5.219	1.99
CR (1) O 3	BD* (1) C 38 - H 66	1352.84	14.72	3.991	1.99
CR (1) O 3	RY* (1) H 70	1319.02	14.37	3.888	1.99
CR (1) O 3	RY* (12) C 36	1254.1	14.99	3.871	1.99
CR (1) O 3	RY* (12) C 38	1075.45	16.69	3.782	1.99
CR (1) O 3	RY* (2) C 39	889.11	16.43	3.415	1.99
LP (1) O 3	RY* (4) O 3	2559.65	0.2	0.64	1.96
LP (1) O 3	RY* (5) C 39	1044.68	0.35	0.542	1.96

to the σ* (C18–C21) and σ* (C20–C25) orbitals with energies of 99.02 and 161.88 kcal mol^{-1}, respectively.

3.6. Evaluation of the molecular electrostatic potentials from electron densities and nuclear charges and nuclear induced chemical shift (NICS) measurements for the analysis of aromaticity

The electrostatic potential (V(r)) around a molecule is generated by its nuclei and electrons. Analysis of static charge distribution is particularly useful for predicting reactivity and can be defined by experimental and computational calculations. Charge distribution indicates the positions or regions of a molecule, to which electrophiles are initially attracted. It can also be used for the analysis of optimal relative orientations of reactants or respective orientations of molecules and their cellular receptors [32,60,61]. Fig. 4 illustrates the possible reaction sites of selpercatinib within the range of −18.02–18.02 Bohr^3. In the figure, colours blue to red correspond to values between −0.100 and 0.100, respectively.

As it can be seen, the blue colour was predominantly noted near the nitrogen and oxygen atoms in selpercatinib. These are electron-rich sites; therefore, they are easily attacked by electrophiles. In contrast, the red colour was mainly observed near carbon atoms of the 2-methylpropan-2-ol-1-oxy, diazobicycloheptane, pyridine, 4-methoxypyridine and methyl moieties. These are electron-poor sites; hence, they are attacked by nucleophiles [62].

The electrostatic potentials determined based on nuclear charges of selpercatinib are shown in Fig. 5 [63–65]. Colours from blue to red refer to numerical values between 0.000 and 50.000. The atomic structure ranged from −19.32 to 19.32 Bohr^3. For nuclear charge between 13 and 17, the blue colour near the proton atoms in 2-methylpropan-2-ol-1-oxy, pyrazolopyridine, carbonitrile, diazobicycloheptane, pyridine and 4-methoxypyridinemethyl groups suggested that these sites were most likely to undergo substitution reactions. Moreover, for nuclear charge between 40 and 50, the red colour near oxygen, nitrogen and carbon atoms in 2-methylpropan-2-ol-1-oxy, pyrazolopyridine, carbonitrile, diazobicycloheptane, pyridine and 4-methoxypyridinemethyl moieties

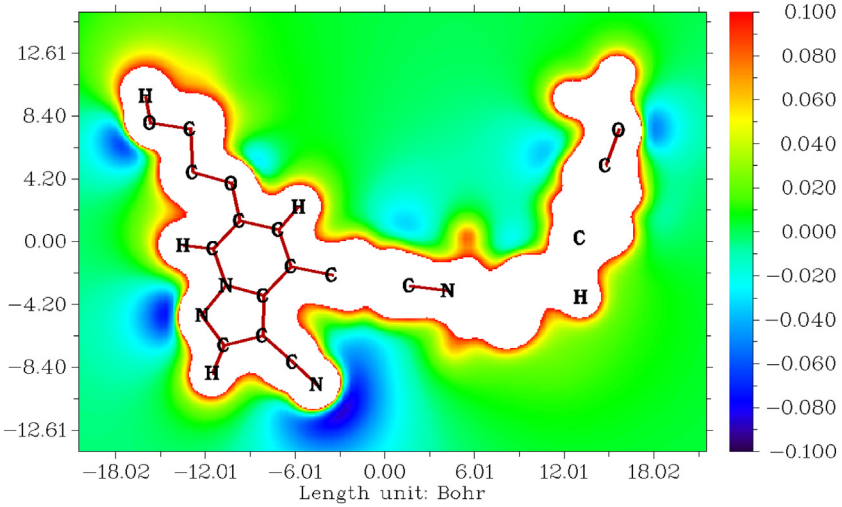

Fig. 4. Molecular electrostatic potentials of selpercatinib.

indicated that these sites predominantly underwent addition reactions. Lastly, for nuclear charge between 27 and 33, the greenish-yellow colour near all other elements implied that these sites were not involved in either addition or substitution reactions.

The NICS analysis involves a magnetic measurement of the local level of ring aromaticity in a molecule [66–70]. Selpercatinib contains one terminal pyridine ring and one pyridine moiety in the middle of the molecule. In addition, the compound also exhibits a pyrazolo-[1,5-a]-pyridine ring, which is a combination of pyridine and pyrazole rings. In this study, NICS(0), NICS (1) and NICS(−1) analyses were performed for all of the above-mentioned aromatic groups at the DFT-B3LYP / 6-31G+(d) level. Several reports demonstrated that NICS (1) is a better measure of magnetic aromaticity that NICS(0), especially in the case of five-membered rings.

The NICS(0), NICS(1) and NICS(−1) values of the terminal pyridine ring in the molecule were determined at −6.95, −9.15 and −9.36, respectively. These values were comparable those pure pyridine (i.e. NICS(1), NICS (1) and NICS(−1) of −6.69, −9.98 and −9.95, respectively). Hence, the results indicated that the pyridine ring in selpercatinib maintained its aromaticity. The NICS(0), NICS(1) and NICS(−1) values of the pyridine ring situated in the middle of the molecule were found to be −5.32, −7.49 and −7.85, respectively. These values evidently demonstrated that the aromaticity of the pyridine ring marginally decreased. The NICS(0), NICS(1) and NICS(−1) values of the pyridine ring of the pyrazolo-[1,5-a]-pyridine system were established at −7.35, −7.43 and −7.44. It is noteworthy that the NICS(1) and NICS(−1) values were consistent with second order degeneracy. Furthermore, the NICS(0), NICS(1) and NICS(−1) values of the five-membered pyrazole ring of the pyrazolo-[1,5-a]-pyridine system were determined at −13.84, −11.16 and −11.20, respectively. Thus, the NICS(1) and NICS(−1) values were consistent with second order degeneracy and showed similar magnetic influence at the studied locations in the molecule. Overall, the pyrazole ring of the pyrazolo-[1,5-a]-pyridine system in selpercatinib was found to be the most aromatic, while the pyridine ring in the centre of the molecule was established as the least aromatic. Specifically, the highest level of aromaticity in the molecule was detected in the centre of the pyrazole ring of the pyrazolo-[1,5-a]-pyridine system. In contrast, the centre of the pyridine ring situated in the middle part of the molecule was comparatively less aromatic.

3.7. Analysis of the average localised ionisation energy of selpercatinib

The average localised ionisation energy, I(r), is the energy needed to remove an electron from point r in the system. The lowest values of I

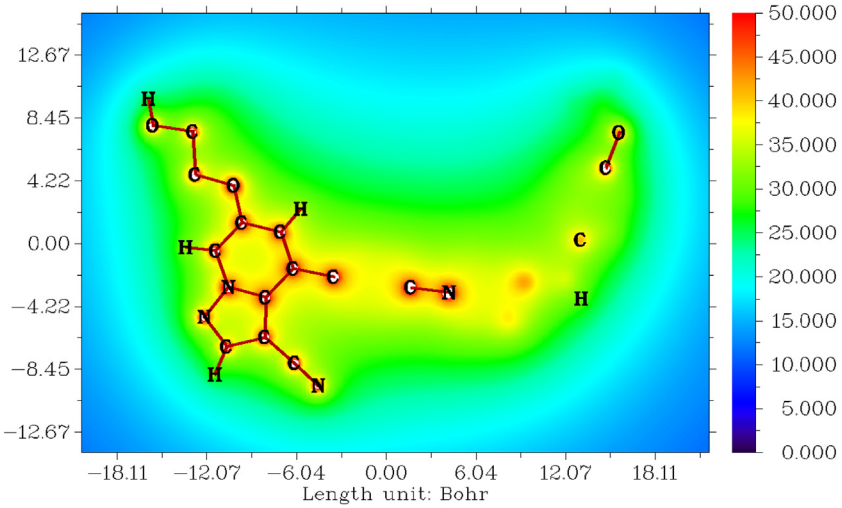

Fig. 5. Molecular electrostatic potentials determined based on nuclear charges of selpercatinib.

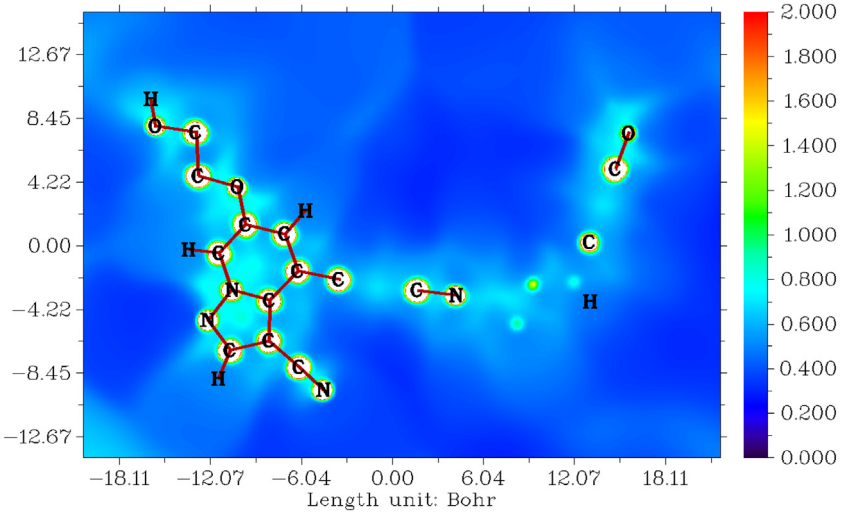

Fig. 6. Average localised ionisation energy of selpercatinib.

(r) indicate the positions exhibiting the least tightly held electrons, i.e. the most likely sites for reactions with electrophiles or radical species. In addition to its importance in predicting reactivity, I(r) plays a significant role in evaluation of the atomic shell composition, electronegativity as well as local polarisability and hardness [71]. Fig. 6 demonstrates the delocalisation and localisation of electrons in selpercatinib within the range between −18.11 and 18.11 Bohr^3. Colours blue to red correspond to numerical values of 0.000–2.000.

The bluish-green colour indicates delocalised electrons of the methoxypyridine, diazobicycloheptane, pyridine, pyrazolopyridine and 2-methylpropan-2-ol-1-oxy groups. These moieties give rise to a number of resonance structures and increase the stability of the molecule. Moreover, blue denotes saturated or sigma bonds between the proton, carbon and oxygen atoms. Red indicates multiple bonds in the molecule; however, no such bonds were detected in selpercatinib.

3.8. Evaluation of non-covalent interactions in selpercatinib

Non-covalent interactions differ from covalent bonds in that they do not involve sharing of electrons. Instead, they involve dispersed variations of electromagnetic interactions between molecules or within a molecule. Non-covalent interactions are important in three-dimensional arrangements of large molecules, such as proteins and nucleic acids. Additionally, they play key roles in various biological processes, in which large molecules bind to each other specifically but transiently. Consideration of covalent interactions is a crucial part of drug and material design as covalent bonds affect crystallinity and self-assembly processes [39]. Fig. 7 shows the non-covalent interactions of selpercatinib, including hydrogen bonds, van der Waals interactions and steric effects. The graph is a plot of energy vs. reduced density gradient.

The hydrogen bonding interactions between the nitrogen atom in the carbonitrile moiety and the hydrogen atoms in pyrazole were detected between −0.021 and −0.005 a.u. Furthermore, the van der Waals forces between the oxygen and hydrogen atoms of the methylpropan-2-ol-1-oxy group in selpercatinib were in energy range of −0.005–0.006 a.u. Lastly, the steric effects between the 2-methylpropan-2-ol-1-oxy and pyrazolpyridine moieties as well as between the diazobicycloheptane and methylpyridine-4-methoxy groups were in the energy range of 0.006–0.024 a.u.

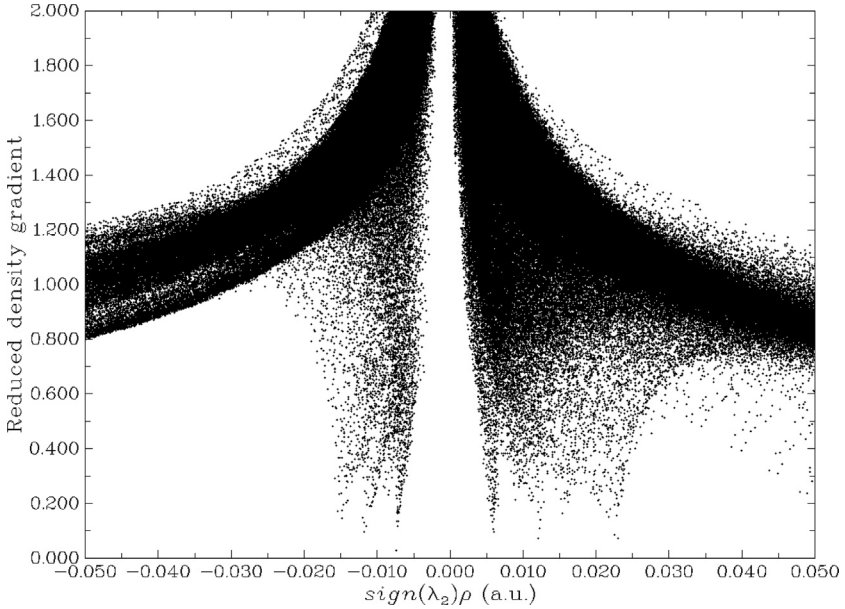

Fig. 7. Non-covalent interactions of selpercatinib.

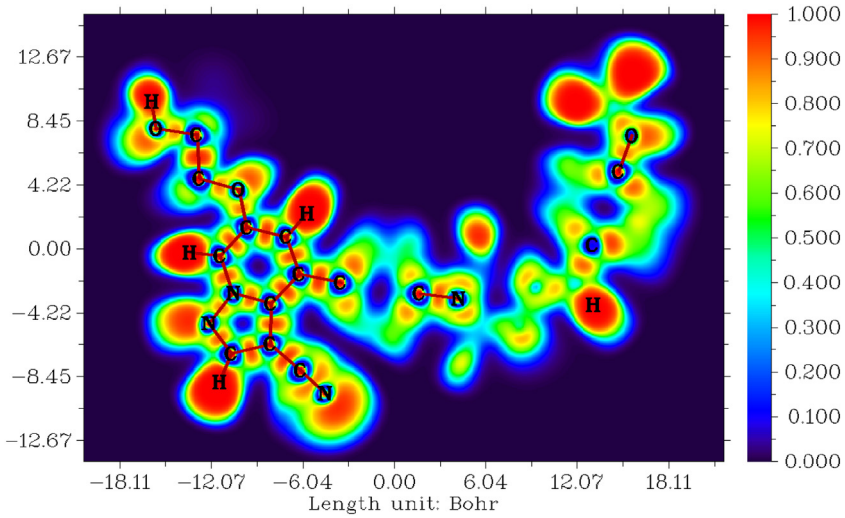

Fig. 8. ELF of selpercatinib.

3.9. Analysis of the electron localisation function (ELF) of selpercatinib

We subsequently investigated the electronic structure of selpercatinib. Higher values of ELF indicate strong localisation, while low values imply strong delocalisation of electrons in a molecule [72–74]. The ELF values of selpercatinib are demonstrated in Fig. 8.

Colours blue to red correspond to numerical values between 0.000 and 0.100 for the molecule within the range of −19.32–19.32 Bohr^3. Red was observed near all protons, lone pairs of electrons on the oxygen and nitrogen atoms as well as near the core orbital electrons of the carbon atoms of the 2-methylpropan-2-ol-1-oxy, pyrazolopyridine, carbonitrile, diazobicycloheptane, pyridine and 4-methoxypyridinemethyl groups, indicating strongly localised electrons. Moderately delocalised electrons were marked in green. These were detected near ring and chain structures in the molecule. Lastly, the blue colour denoted strongly delocalised electrons at the carbon-to-nitrogen-to-carbon positions in the 2-methylpropan-2-ol-1-oxy and carbonitrile chains as well as in the pyrazolopyridine, diazobicycloheptane, pyridine and 4-methoxypyridinemethyl groups. Electron delocalisation resulted in a number of resonance structures, which contributed to the stability of selpercatinib.

3.10. Localised orbital locator (LOL) of selpercatinib

We subsequently analysed the localised and delocalised molecular orbitals of selpercatinib [75–77]. The LOL profile for selpercatinib is shown in Fig. 9.

Colours blue to red correspond to numerical values between 0.000 and 0.800 for the molecule within the range of −19.32–19.32 Bohr^3. The blue colour denotes weakly pi-delocalised orbitals, whereas red indicates strongly pi-delocalised orbitals in selpercatinib. In the molecule, these orbitals are adjacent to one another; therefore, delocalisation of electrons occurs on oxygen, nitrogen and carbon atoms of the 2-methylpropan-2-ol-1-oxy, pyrazolopyridine, carbonitrile, diazobicycloheptane, pyridine and 4-methoxypyridinemethyl groups.

3.11. Reduced density gradient of selpercatinib

The reduced density gradient is directly proportional to the electronic density of a molecule. Low value of the reduced density gradient indicates low electronic density [75–77]. Fig. 10 shows the reduced density gradient of selpercatinib.

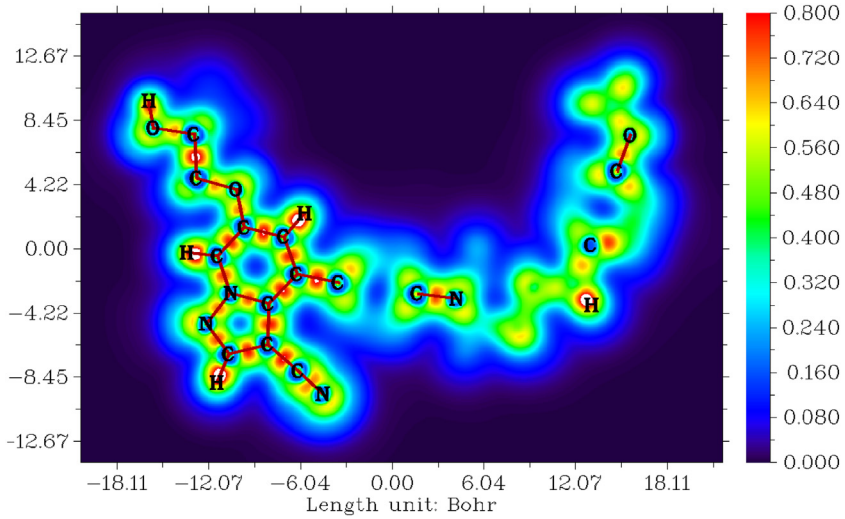

Fig. 9. LOL profile of selpercatinib.

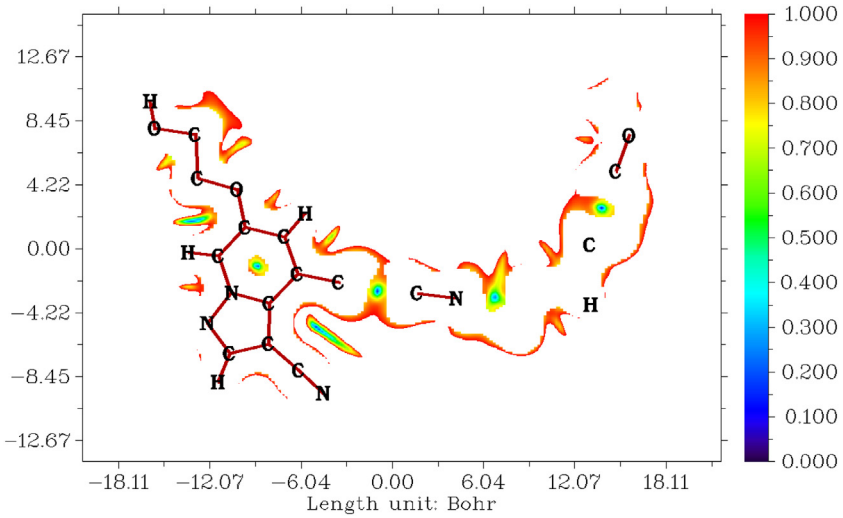

Fig. 10. Reduced density gradient of selpercatinib.

Colours blue to red correspond to numerical values between 0.000 and 1.000 for the molecule within the range of −19.32–19.32 Bohr^3. In the plot, red indicates the reduced density between 0.9000 and 1.000 for the nitrogen atoms of the 2-methylpropan-2-ol-1-oxy, pyrazolopyridine, carbonitrile, diazobicycloheptane, pyridine and 4-methoxypyridinemethyl groups. The low reduced density gradients are denoted in green and blue (0.5–0.65 and 0.0–0.5, respectively). As shown in Fig. 10, the low and high reduced density gradients are mixed.

3.12. Local information entropy of selpercatinib

Local information entropy analysis provides information on the stability of a molecule. Entropy is a feature of probability distributions and can be used to quantify uncertainty. High values of local information entropy are directly proportional to the uncertainty of spatial distribution of electrons [78–81]. Fig. 11 demonstrates the local information entropy of selpercatinib.

Colours blue to red correspond to numerical values between 0.000 and 1.000 for the molecule within the range of −19.32–19.32 Bohr^3. As it can be seen, all elements in the selpercatinib molecule exhibit very low local information entropy (0.000–0.100). This suggests that selpercatinib is more stable at low uncertainty of spatial distribution of electrons denoted in blue and depends on the mass of hydrogen, carbon, nitrogen and oxygen atoms.

3.13. Proton affinity and regioselectivity of monoprotonation of selpercatinib

Selpercatinib contains seven nitrogen atoms and exhibits remarkably high gas phase proton affinity. However, as they are located in different environments, the gas phase proton affinities corresponding to different nitrogen atoms vary. The structure of the molecule contains two nitrogen atoms (N4 and N5) in the 3,6-diazabicyclo-[3.1.1]-heptane ring and two (N6 and N7) in the pyridine moieties. Moreover, there are two nitrogen atoms (N8 and N9) in the substituents of the pyrazolo-[1,5-a]-pyridine system and one (N10) in the cyano functionality bonded to this scaffold. The proton affinities corresponding to these six nitrogen atoms were calculated using DFT with the B3LYP functional combined with the 6-31G(d) basis set. Fig. 7 shows the comparison of the gas phase proton affinities of the different nitrogen atoms in selpercatinib.

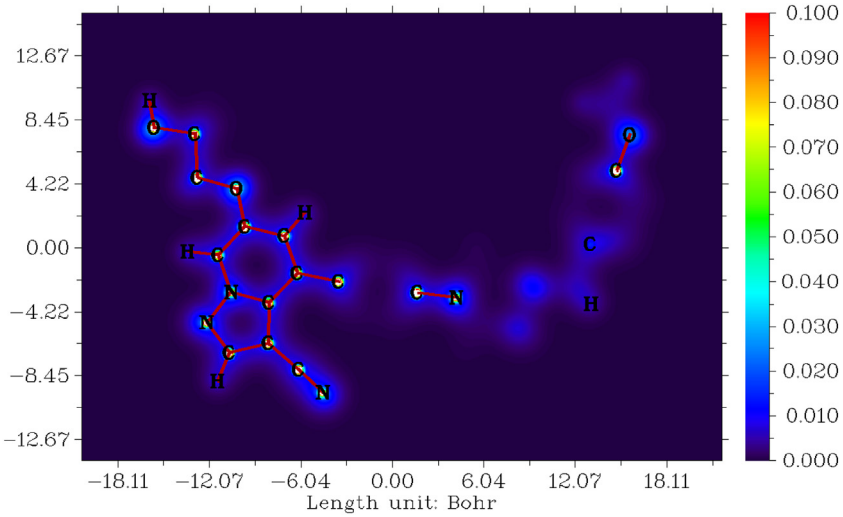

Fig. 11. Local information entropy of selpercatinib.

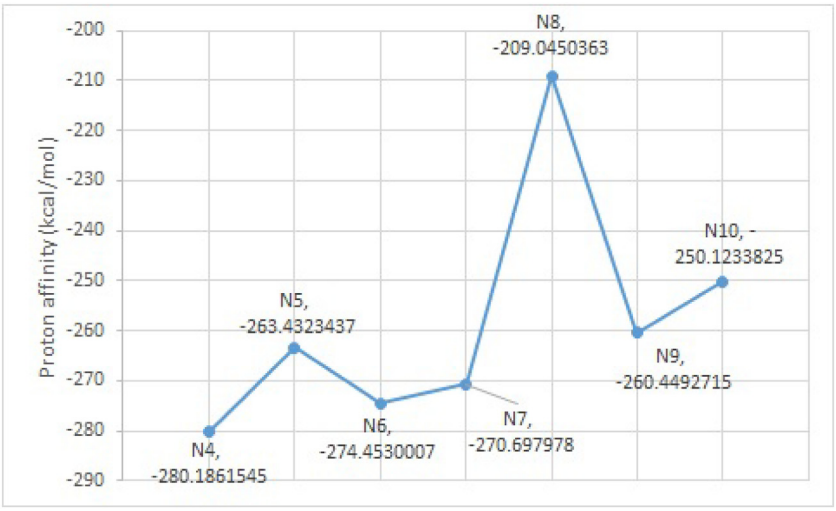

Fig. 12. Comparison of the gas phase proton affinities (kcal mol^{-1}) corresponding to the seven nitrogen atoms in selpercatinib.

Fig. 12 clearly indicates that N4, i.e. one of the nitrogen atoms of the 3,6-diazabicyclo-[3.1.1]-heptane system, exhibits the highest gas phase proton affinity, followed by the N6 atom of the pyridine ring in the centre of the molecule, N7 of the other pyridine ring, N5, i.e. the other nitrogen atom of the 3,6-diazabicyclo-[3.1.1]-heptane system, N9 of the pyrazole ring and N10 of the cyano moiety. Moreover, N8, i.e. one of the nitrogen atoms of the pyrazolo-[1,5-a]-pyridine system was found to display the lowest gas phase proton affinity. Thus, the gas phase proton affinity of the seven nitrogen atoms of selpercatinib was in the order of N4 > N6 > N7 > N5 > N9 > N10 > N8.

Notably, N4 is not attached to any aromatic system and exhibits a natural pyramidal geometry, making its lone electron pair easily available. This was the reason for the highest gas phase proton affinity of this atom. Furthermore, N6 and N7 of the pyridine rings also show high gas phase proton affinities. Similarly to N4, the lone electron pairs of N6 and N7 are not delocalised into any aromatic system. In contrast, N5 displays a comparatively low gas phase proton affinity as it is directly attached to the central pyridine ring of the molecule. Consequently, its lone pair of electrons participates in resonance with the pyridine ring. In the case of N9, the lone pair of electrons participates in aromaticity, decreasing the gas phase proton affinity of this nitrogen atom. The sp. hybridised nitrogen atom of the cyano moiety (N10) shows an even lower gas phase proton affinity as its lone pair of electrons is held tightly. Moreover, the considerably lower gas phase proton affinity of N8 is attributed to the protonation of the atom at the cost of distortion of the structure of the stable bicyclic aromatic rings. Hence, the monoprotonation of selpercatinib was found to be regioselective at the N4 position.

3.14. Ion selectivity and zinc affinity of selpercatinib

The gas phase affinities of N4 towards s-block metal ions, including Li^+, Na^+ and K^+, were subsequently calculated at the same theoretical level. Fig. 13 shows the comparison of the gas phase metal ion affinities and gas phase proton affinity at the N4 position.

Fig. 13 clearly indicates the high chemoselectivity of the N4 atom towards H^+. The gas phase affinity decreases sharply from H^+ to Li^+. Moreover, the gas phase affinities were found slightly decrease with the decrease in the charge density from Li^+ to K^+ via Na^+. The affinities of selpercatinib towards Zn^{++} were calculated at the DFT-B3LYP/LanL2DZ level both in gas phase and in presence of water using the IEFPCM model. When the Zn^{++} ion was placed close to N4 and N5, the gas phase affinity was established at −254.91 kcal mol^{-1}. In presence of water in the IEFPCM model, at the same position of Zn^{++}, the affinity

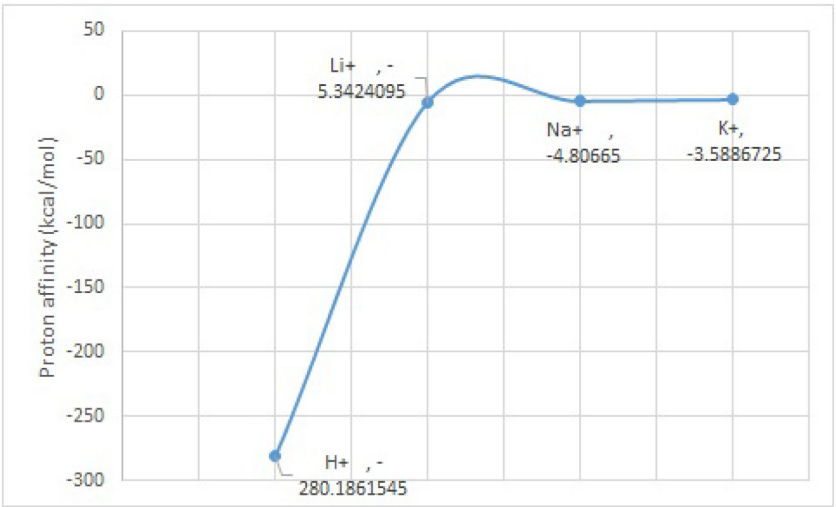

Fig. 13. Comparison of the gas phase affinities (kcal mol^{-1}) of N4 of selpercatinib towards H^+, Li^+, Na^+ and K^+.

Table 5
Docking results for selpercatinib with SARS-CoV-2 proteins.

Parameters	6LZG	6 W63	6 M03	6 LU7
Energy	145.853 kcal mol^{-1}	139.788 kcal mol^{-1}	153.313 kcal mol^{-1}	153.362 kcal mol^{-1}
Simple Fitness	145.853 kcal mol^{-1}	139.788 kcal mol^{-1}	153.313 kcal mol^{-1}	153.362 kcal mol^{-1}
Full Fitness	−3319.6 kcal mol^{-1}	−1057.9 kcal mol^{-1}	−1059.3 kcal mol^{-1}	−1083.8 kcal mol^{-1}
Inter Full Fitness	−82.67 kcal mol^{-1}	−58.331 kcal mol^{-1}	−51.705 kcal mol^{-1}	−45.918 kcal mol^{-1}
Intra Full Fitness	187.894 kcal mol^{-1}	186.294 kcal mol^{-1}	189.101 kcal mol^{-1}	190.347 kcal mol^{-1}
Solvent Full Fitness	−3957 kcal mol^{-1}	−1407.1 kcal mol^{-1}	−1417.6 kcal mol^{-1}	−1447.7 kcal mol^{-1}
Surface Full Fitness	532.146 kcal mol^{-1}	221.238 kcal mol^{-1}	220.891 kcal mol^{-1}	219.475 kcal mol^{-1}
Extra Full Fitness	0 kcal mol^{-1}	0 kcal mol^{-1}	0 kcal mol^{-1}	0 kcal mol^{-1}
ΔG complex solvent polar	−3957 kcal mol^{-1}	−1407.1 kcal mol^{-1}	−1417.6 kcal mol^{-1}	−1447.7 kcal mol^{-1}
ΔG complex solvent nonpolar	532.146 kcal mol^{-1}	221.238 kcal mol^{-1}	220.891 kcal mol^{-1}	219.475 kcal mol^{-1}
ΔG protein solvent polar	−3956. kcal mol^{-1}	−1372.1 kcal mol^{-1}	−1385.7 kcal mol^{-1}	−1411.4 kcal mol^{-1}
ΔG protein solvent nonpolar	533.989 kcal mol^{-1}	222.123 kcal mol^{-1}	221.3 kcal mol^{-1}	221.095 kcal mol^{-1}
ΔG ligand solvent polar	−61.14 kcal mol^{-1}	−60.313 kcal mol^{-1}	−61.442 kcal mol^{-1}	−59.367 kcal mol^{-1}
ΔG ligand solvent nonpolar	11.2274 kcal mol^{-1}	11.2051 kcal mol^{-1}	11.3135 kcal mol^{-1}	11.0969 kcal mol^{-1}
ΔG van der Waals force	−82.67 kcal mol^{-1}	−58.331 kcal mol^{-1}	−51.705 kcal mol^{-1}	−45.918 kcal mol^{-1}
ΔG electric force	0 kcal mol^{-1}	0 kcal mol^{-1}	0 kcal mol^{-1}	0 kcal mol^{-1}
Total ΔG	−9.3169 kcal mol^{-1}	−9.1002 kcal mol^{-1}	−8.1853 kcal mol^{-1}	−8.1222 kcal mol^{-1}

drastically decreased, reaching values as low as −23.11 kcal mol^{-1}. The decrease in the affinity of selpercatinib towards Zn^{++} in the presence of water was attributed to the coordination and entrapment of the metal ion in the solvent envelope. The coordinated cation is bulkier, which results in the reduced affinity of selpercatinib towards it.

3.15. Molecular docking

The molecular docking analysis was used to evaluate the interactions between selpercatinib and SARS-CoV-2 proteins, including PDB IDs 6LZG [82], 6 W63 [83], 6 M03 [83] and 6 LU7. Numerous binding interactions with the residues of these proteins have been identified [84].

Table 5 summarises the docking results obtained from SwissDock, including the energy of the interactions between selpercatinib and the studied proteins. As it can be seen, SARS-CoV-2 protein 6LZG exhibited higher full fitness, inter full fitness, solvent full fitness, surface full fitness, ΔG of the complex in a polar solvent, ΔG of the complex in a nonpolar solvent, ΔG of the protein in a polar solvent, ΔG of the protein in a nonpolar solvent, ΔG of the ligand in a nonpolar solvent, ΔG of the van der Waals forces and total ΔG energy than the other investigated proteins. In contrast, protein 6 M03 displayed higher ΔG of the ligand in a polar solvent compared to the other proteins, while 6 LU7 showed the highest energy as well as simple and intra full fitness energies [85–89]. SARS-CoV-2 proteins 6LZG, 6 W63, 6 M03 and 6 LU7 exhibited full fitness energies of −3319.61, −1057.90, −1059.33 and −1083 kcal mol^{-1}, respectively. The total ΔG values were determined at −9.3169, −9.1002, −8.1853 and −8.1222 kcal mol^{-1}, respectively.

Analysis of the SARS-CoV proteins 6LZG, 6 W63, 6 M03 and 6 LU7 using PatchDock enabled the determination of score values of 6508, 5570, 5624 and 5894, respectively. Furthermore, the total interacting

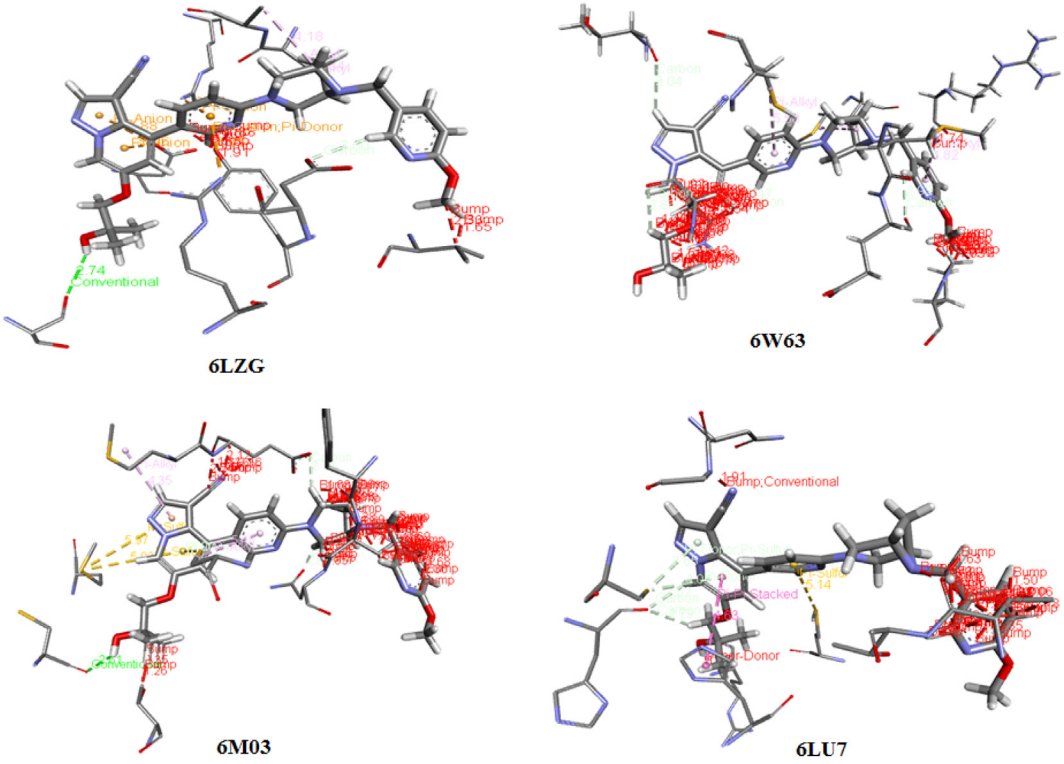

Fig. 14. Skeletal structures showing the interactions between selpercatinib and SARS-CoV-2 proteins.

surface areas were established at 745.50, 688.10, 770.40 and 743.80 Å^2, respectively, while the minimum atomic contact energies were −22.58, −331.05, −409.25 and 372.48 kcal mol^{-1}, correspondingly [90–92]. In addition, the molecule solvent accessibilities were found to be 3385.80, 3089.51, 2833.11 and 3009.17 Å^2, respectively.

Fig. 14 shows the skeletal structures of the interactions between selpercatinib and SARS-CoV-2 proteins. Additionally, **Fig. S2** demonstrates the interactions between selpercatinib and SARS-CoV-2 protein residues, whereas **Table S1** summarises the SARS-CoV-2 protein labels, names, hydrophobicity, pKa, average isotropic displacement, secondary structure, residue solvent accessibility, side-chain solvent accessibility, percent solvent accessibility, and percent side-chain solvent accessibility.

Table S2 shows the non-covalent interactions between selpercatinib and SARS-CoV-2 proteins, including favorable non-bonding as well as unfavourable non-bonding and bonding interactions. Moreover, Table 6 summarises the hydrophobicity, hydrophilicity as well as neutral, acidic and basic groups participating in the interactions between selpercatinib and SARS-CoV-2 proteins.

Fig. S3, Tables 5 and 6 summarise the hydrophobic interactions between selpercatinib and SARS-CoV-2 proteins. In addition, hydrophilic interactions between selpercatinib and SARS-CoV-2 proteins are demonstrated in **Fig. S4**, Tables 5 and 6. The neutral, acidic and basic groups participating in the interactions between selpercatinib and SARS-CoV-2 proteins are shown in Tables 5, 6 and **Fig. S5–S7**.

Table 6
Non-bonding interactions between selpercatinib and SARS-CoV-2 protein residues.

Non-bonding interactions	Name of the SARS-CoV-2 proteins	Labels of the SARS-CoV-2 proteins
Hydrophobicity	6LZG	GLU A:37, MET A:383, ALA A:386, ALA A:387, PHE A:390, ARG A:393, ARG B:403, ASP B:405 SER B:494, VAL B:503, and TYR B:505
	6 W63	THR A:26, MET A:49, LEU A:141, ASN A:142, CYS A:145, MET A:165, GLU A:166, LEU A:167, PRO A:168, and ARG A:188
	6 M03	THR A:25, LEU A:27, VAL A:42, CYS A:44, MET A:49, PHE A:140, LEU A:141, ASN A:142, CYS A:145, MET A:165, GLU A:166, and LEU A:167
	6 LU7	CYS A:22, THR A:24, THR A:25, LEU A:27, HIS A:41, CYS A:44, MET A:49, LEU A:141, ASN A:142, GLY A:143, CYS A:145, HIS A:164, MET A:165, VAL A:186, and ARG A:188
Hydrophilicity	6LZG	ASN A:33, HIS A:34, GLU A:37, ASP A:38, LYS A:353, GLN A:388, ARG A:393, ARG B:403, ASP B:405, GLN B:493, SER B:494, and TYR B:505
	6 W63	THR A:26, HIS A:41, ASN A:142, HIS A:164, GLU A:166, PRO A:168, ASP A:187, ARG A:188, GLN A:189, and GLN A:192
	6 M03	THR A:25, HIS A:41, ASN A:142, HIS A:163, HIS A:164, GLU A:166, HIS A:172, and GLN A:189
	6 LU7	THR A:24, THR A:25, HIS A:41, ASN A:142, GLY A:143, HIS A:164, GLU A:166, ASP A:187, ARG A:188, GLN A:189, and GLN A:192
Neutral groups	6LZG	THR A:324, PRO A:389, TYR B:453, SER B:494, TYR B:495, GLY B:496, GLY B:502, GLY B:504, and TYR B:505
	6 W63	THR A:A25, THR A:26, GLY A:143, PRO A:168, and THR A:190
	6 M03	THR A:25, SER A:46, TYR A:118, SER A:139, GLY A:143, and SER A:144
	6 LU7	GLY A:23, THR A:24, THR A:25, THR A:26, THR A:45, THR A:54, GLY A:143, and SER A:144
Acidic groups	6LZG	GLU A:37, ASP A:38, and ASP B:405
	6 W63	GLU A:166, and ASP A:187
	6 M03	GLU A:166
	6 LU7	GLU A:166, and ASP A:187
Basic groups	6LZG	HIS A:34, LYS A:353, ARG A:393, and ARG B:403
	6 W63	HIS A:41, HIS A:164, and ARG A:188
	6 M03	HIS A:41, HIS A:163, HIS A:164, and HIS A:172
	6 LU7	HIS A:41, HIS A:164, and ARG A:188

4. Conclusions

Selpercatinib exhibits suitable HOMO–LUMO energy gap values. The molecule also displays good chemical parameters, ionisation energy, electron affinity, global hardness, global softness, chemical potential, electronegativity, electrophilicity index and nucleophilicity index. The UV–vis spectrum of selpercatinib showed absorption peaks at 307.1098 and 272.1917 nm with 0.0.4698 and 101,061 oscillator strengths, respectively. Analysis of the NLO properties of the molecule revealed that its dipole moment is 0.9950 times greater than that of urea and 3.6106 times higher than that of *p*-nitroacetanilide. Moreover, it was determined that hyperpolarisability of selpercatinib is 42.0605 times higher than that of urea and 4.6058 times higher than that of *p*-nitroacetanilide. The mean polarisability is 17.4480 and 3.45 times greater than those of urea and *p*-nitroacetanilide, respectively. It was also established that the anisotropy of the polarisability of the compound is 17.91 and 2.7533 times higher than those of urea and *p*-nitroacetanilide, correspondingly. Lastly, it was found that the molar refractivity of selpercatinib is 17.448 and 3.4512 times higher than those of urea and *p*-nitroacetanilide, respectively. The NBO analysis was used to evaluate the bonding molecular orbital properties of selpercatinib exhibiting suitable occupancies and energies. The assessed reaction site properties included electrostatic potentials, average localised ionisation energy and noncovalent interactions. It was determined that the methoxy, methylpyridine, 3,6-diazobicycloheptane, pyridine, carbonitrile and pyrazolopyridine moieties were the most reactive groups in selpercatinib. The molecule was shown to behave as a proton sponge and displayed strong proton affinity. Furthermore, selpercatinib is capable of removing metal ions in aqueous solutions. The particularly noteworthy ability is its attraction to zinc ions in solutions. It is know than as zinc ions play key roles in preventing the penetration of viruses into human cells; however, due to their charge, they cannot enter the cells through the lipid bilayers. Importantly, the affinity of selpercatinib towards zinc makes it an ionophore, enabling effective transport of active zinc ions into cells. Lastly, we conducted a molecular docking analysis to investigate the interactions between selpercatinib and several SARS-CoV-2 proteins (6LZG, 6 W63, 6 M03, and 6 LU7). The interactions between hydrophilic, hydrophobicity, acidic, basic and neutral groups of the proteins and selpercatinib were evaluated in detail.

Declaration of Competing Interest

Authors declare no conflicts of interest.

Acknowledgement

The authors extend their appreciation to the Deanship of Scientific Research, King Saud University for funding this work through research group no (RG-1440-141).

Appendix A. Supplementary data

Supplementary data to this article can be found online at https://doi.org/10.1016/j.molliq.2020.114765.

References

[1] R. Şentürk, Y. Wang, A.H. Schinkel, J.H. Beijnen, R.W. Sparidans, Quantitative bioanalytical assay for the selective RET inhibitors selpercatinib and pralsetinib in mouse plasma and tissue homogenates using liquid chromatography-tandem mass spectrometry, J. Chromatogr. B 1147 (2020) 122131, https://doi.org/10.1016/j.jchromb.2020.122131.

[2] Z. Qiu, B. Ye, K. Wang, P. Zhou, S. Zhao, W. Li, P. Tian, Unique genetic characteristics and clinical prognosis of female patients with lung Cancer harboring RET fusion gene, Sci. Rep. 10 (2020) 10387, https://doi.org/10.1038/s41598-020-66883-0.

[3] B.J. Solomon, L. Tan, J.J. Lin, S.Q. Wong, S. Hollizeck, K. Ebata, B.B. Tuch, S. Yoda, J.F. Gainor, L.V. Sequist, G.R. Oxnard, O. Gautschi, A. Drilon, V. Subbiah, C. Khoo, E.Y.

Zhu, M. Nguyen, D. Henry, K.R. Condroski, G.R. Kolakowski, E. Gomez, J. Ballard, A.T. Metcalf, J.F. Blake, S.J. Dawson, W. Blosser, L.F. Stancato, B.J. Brandhuber, S. Andrews, B.G. Robinson, S.M. Rothenberg, RET solvent front mutations mediate acquired resistance to selective RET inhibition in RET-driven malignancies, J. Thorac. Oncol. 15 (2020) 541–549, https://doi.org/10.1016/j.jtho.2020.01.006.

[4] W. Kian, D. Levitas, W. Alguayn, W. Shalata, A.A. Sharb, D. Levin, L.C. Roisman, M. Tokar, N. Peled, A. Yakobson, Hypercalcemia as a rebound phenomenon of LOXO-292 efficacy in medullary thyroid cancer, JTO Clin. Res. Rep. 1 (2020) https://doi.org/10.1016/j.jtocrr.2020.100002.

[5] R. Pirker, M. Filipits, Alectinib in RET-rearranged non-small cell lung cancer-another progress in precision medicine? Transl. Lung Cancer Res. 4 (2015) 797–800, https://doi.org/10.3978/j.issn.2218-6751.2015.03.08.

[6] S. Su, G. Wong, W. Shi, J. Liu, A.C.K. Lai, J. Zhou, W. Liu, Y. Bi, G.F. Gao, Epidemiology, genetic recombination, and pathogenesis of coronaviruses, Trends Microbiol. 24 (2016) 490–502, https://doi.org/10.1016/j.tim.2016.03.003.

[7] K.-S. Yuen, Z.-W. Ye, S.-Y. Fung, C.-P. Chan, D.-Y. Jin, SARS-CoV-2 and COVID-19: the most important research questions, Cell Biosci. 10 (2020) 40, https://doi.org/10.1186/s13578-020-00404-4.

[8] Z. Xu, L. Shi, Y. Wang, J. Zhang, L. Huang, C. Zhang, S. Liu, P. Zhao, H. Liu, L. Zhu, Y. Tai, C. Bai, T. Gao, J. Song, P. Xia, J. Dong, J. Zhao, F.-S. Wang, Pathological findings of COVID-19 associated with acute respiratory distress syndrome, Lancet Respir. Med. 8 (2020) 420–422, https://doi.org/10.1016/S2213-2600(20)30076-X.

[9] M.A. Lake, What we know so far: COVID-19 current clinical knowledge and research, Clin. Med. 20 (2020) 124–127, https://doi.org/10.7861/clinmed.2019-coron.

[10] R. Wu, L. Wang, H.-C.D. Kuo, A. Shannar, R. Peter, P.J. Chou, S. Li, R. Hudlikar, X. Liu, Z. Liu, G.J. Poiani, L. Amorosa, L. Brunetti, A.-N. Kong, An update on current therapeutic drugs treating COVID-19, Curr. Pharmacol. Reports. 6 (2020) 56–70, https://doi.org/10.1007/s40495-020-00216-7.

[11] F. Touret, X. de Lamballerie, Of chloroquine and COVID-19, Antivir. Res. 177 (2020) 104762, https://doi.org/10.1016/j.antiviral.2020.104762.

[12] Y. Wang, D. Zhang, G. Du, R. Du, J. Zhao, Y. Jin, S. Fu, L. Gao, Z. Cheng, Q. Lu, Y. Hu, G. Luo, K. Wang, Y. Lu, H. Li, S. Wang, S. Ruan, C. Yang, C. Mei, Y. Wang, D. Ding, F. Wu, X. Tang, X. Ye, Y. Ye, B. Liu, J. Yang, W. Yin, A. Wang, G. Fan, F. Zhou, Z. Liu, X. Gu, J. Xu, L. Shang, Y. Zhang, L. Cao, T. Guo, Y. Wan, H. Qin, Y. Jiang, T. Jaki, F.G. Hayden, P.W. Horby, B. Cao, C. Wang, Remdesivir in adults with severe COVID-19: a randomised, double-blind, placebo-controlled, multicentre trial, Lancet. 395 (2020) 1569–1578, https://doi.org/10.1016/S0140-6736(20)31022-9.

[13] D.A. Dixon, D. Feller, K.A. Peterson, Chapter one - a practical guide to reliable first principles computational thermochemistry predictions across the periodic table, in: R.A.B.T.-A.R, in: C.C. Wheeler (Ed.), Annu. Rep. Comput. Chem, Elsevier 2012, pp. 1–28, https://doi.org/10.1016/B978-0-444-59440-2.00001-6.

[14] S. Grimme, P.R. Schreiner, Computational chemistry: the fate of current methods and future challenges, Angew. Chem. Int. Ed. 57 (2018) 4170–4176, https://doi.org/10.1002/anie.201709943.

[15] M.K. Varghese, R. Thomas, N.V. Unnikrishnan, C. Sudarsanakumar, Molecular dynamics simulations of xDNA, Biopolym. Orig. Res. Biomol. 91 (2009) 351–360.

[16] A. Matondo, R. Thomas, P.V. Tsalu, C.T. Mukeba, V. Mudogo, α-methylation and α-fluorination electronic effects on the regioselectivity of carbonyl groups of uracil by H and triel bonds in the interaction of U, T and 5FU with HCl and TrH 3 (Tr = B, Al), J. Mol. Graph. Model. 88 (2019) 237–246, https://doi.org/10.1016/j.jmgm.2019.02.006.

[17] Z. Ullah, R. Thomas, Mechanistic insights can resolve the low reactivity and selectivity issues in intermo-lecular Rauhut Currier (RC) reaction of γ-hydroxyenone, New J. Chem. (2020)https://doi.org/10.1039/D0NJ02732D.

[18] D.J.F.M.J. Frisch, G.W. Trucks, H.B. Schlegel, G.E. Scuseria, M.A. Robb, J.R. Cheeseman, G. Scalmani, V. Barone, G.A. Petersson, H. Nakatsuji, X. Li, M. Caricato, A. Marenich, J. Bloino, B.G. Janesko, R. Gomperts, B. Mennucci, H.P. Hratchian, J.V. Ort, Gaussian09W Revision D.01, 2009.

[19] M. Orio, D.A. Pantazis, F. Neese, Density functional theory, Photosynth. Res. 102 (2009) 443–453, https://doi.org/10.1007/s11120-009-9404-8.

[20] P.J. Stephens, F.J. Devlin, C.F. Chabalowski, M.J. Frisch, Ab initio calculation of vibrational absorption and circular dichroism spectra using density functional force fields, J. Phys. Chem. 98 (1994) 11623–11627, https://doi.org/10.1021/j100096a001.

[21] R. Krishnan, J.S. Binkley, R. Seeger, J.A. Pople, Self-consistent molecular orbital methods. XX. A basis set for correlated wave functions, J. Chem. Phys. 72 (1980) 650–654, https://doi.org/10.1063/1.438955.

[22] J.B. Foresman, Ae. Frisch, I. Gaussian, Exploring Chemistry with Electronic Structure Methods, Gaussian, Inc, 1996.

[23] K. Okuno, Y. Shigeta, R. Kishi, H. Miyasaka, M. Nakano, Tuned CAM-B3LYP functional in the time-dependent density functional theory scheme for excitation energies and properties of diarylethene derivatives, J. Photochem. Photobiol. A Chem. 235 (2012) 29–34, https://doi.org/10.1016/j.jphotochem.2012.03.003.

[24] T. Yanai, D.P. Tew, N.C. Handy, A new hybrid exchange–correlation functional using the coulomb-attenuating method (CAM-B3LYP), Chem. Phys. Lett. 393 (2004) 51–57, https://doi.org/10.1016/J.CPLETT.2004.06.011.

[25] N.M. O'boyle, A.L. Tenderholt, K.M. Langner, CCLIB: a library for package-independent computational chemistry algorithms, J. Comput. Chem. 29 (2008) 839–845, https://doi.org/10.1002/jcc.20823.

[26] T. Lu, F. Chen, Multiwfn: a multifunctional wavefunction analyzer, J. Comput. Chem. 33 (2012) 580–592, https://doi.org/10.1002/jcc.22885.

[27] S.K. Burley, H.M. Berman, C. Bhikadiya, C. Bi, L. Chen, L. Di Costanzo, C. Christie, K. Dalenberg, J.M. Duarte, S. Dutta, Z. Feng, S. Ghosh, D.S. Goodsell, R.K. Green, V. Guranović, D. Guzenko, B.P. Hudson, T. Kalro, Y. Liang, R. Lowe, H. Namkoong, E. Peisach, I. Periskova, A. Prlić, C. Randle, A. Rose, P. Rose, R. Sala, M. Sekharan, C. Shao, L. Tan, Y.-P. Tao, Y. Valasatava, M. Voigt, J. Westbrook, J. Woo, H. Yang, J. Young, M. Zhuravleva, C. Zardecki, RCSB Protein Data Bank: biological macromolecular structures enabling research and education in fundamental biology, biomedicine, biotechnology and energy, Nucleic Acids Res. 47 (2018) D464–D474, https://doi.org/10.1093/nar/gky1004.

[28] A. Grosdidier, V. Zoete, O. Michielin, SwissDock, a protein-small molecule docking web service based on EADock DSS, Nucleic Acids Res. 39 (2011) W270–W277, https://doi.org/10.1093/nar/gkr366.

[29] A. Grosdidier, V. Zoete, O. Michielin, Fast docking using the CHARMM force field with EADock DSS, J. Comput. Chem. 32 (2011) 2149–2159, https://doi.org/10.1002/jcc.21797.

[30] E. Mashiach, D. Schneidman-Duhovny, A. Peri, Y. Shavit, R. Nussinov, H.J. Wolfson, An integrated suite of fast docking algorithms, Proteins Struct. Funct. Bioinforma. 78 (2010) 3197–3204, https://doi.org/10.1002/prot.22790.

[31] D. Schneidman-Duhovny, Y. Inbar, R. Nussinov, H.J. Wolfson, PatchDock and SymmDock: servers for rigid and symmetric docking, Nucleic Acids Res. 33 (2005) W363–W367, https://doi.org/10.1093/nar/gki481.

[32] P. Politzer, P.R. Laurence, K. Jayasuriya, Molecular electrostatic potentials: an effective tool for the elucidation of biochemical phenomena, Environ. Health Perspect. 61 (1985) 191–202, https://doi.org/10.1289/ehp.8561191.

[33] J.S. Al-Otaibi, Y.S. Mary, Y.S. Mary, R. Thomas, Quantum mechanical and photovoltaic studies on the cocrystals of hydrochlorothiazide with isonazid and malonamide, J. Mol. Struct. 1197 (2019) 719–726, https://doi.org/10.1016/j.molstruc.2019.07.110.

[34] J.S. Al-Otaibi, Y. Sheena Mary, Y. Shyma Mary, C.Y. Panicker, R. Thomas, Cocrystals of pyrazinamide with p-toluenesulfonic and ferulic acids: DFT investigations and molecular docking studies, J. Mol. Struct. 1175 (2019) 916–926, https://doi.org/10.1016/j.molstruc.2018.08.055.

[35] R. Parthasarathi, V. Subramanian, D.R. Roy, P.K. Chattaraj, Electrophilicity index as a possible descriptor of biological activity, Bioorg. Med. Chem. 12 (2004) 5533–5543, https://doi.org/10.1016/j.bmc.2004.08.013.

[36] L.R. Domingo, M. Ríos-Gutiérrez, P. Pérez, Applications of the conceptual density functional theory indices to organic chemistry reactivity, Molecules. 21 (2016) 748, https://doi.org/10.3390/molecules21060748.

[37] A. Malek, R. Balawender, Revisiting the chemical reactivity indices as the state function derivatives. The role of classical chemical hardness, J. Chem. Phys. 142 (2015) 54104, https://doi.org/10.1063/1.4906555.

[38] H.K. Srivastava, F.A. Pasha, P.P. Singh, Atomic softness-based QSAR study of testosterone, Int. J. Quantum Chem. 103 (2005) 237–245, https://doi.org/10.1002/qua.20506.

[39] P. Politzer, J.S. Murray, An Occam's razor approach to chemical hardness: lex parsimoniae, J. Mol. Model. 24 (2018) 332, https://doi.org/10.1007/s00894-018-3864-8.

[40] M.E. Casida, C. Jamorski, K.C. Casida, D.R. Salahub, Molecular excitation energies to high-lying bound states from time-dependent density-functional response theory: characterization and correction of the time-dependent local density approximation ionization threshold, J. Chem. Phys. 108 (1998) 4439–4449, https://doi.org/10.1063/1.475855.

[41] R. Bauernschmitt, R. Ahlrichs, Treatment of electronic excitations within the adiabatic approximation of time dependent density functional theory, Chem. Phys. Lett. 256 (1996) 454–464, https://doi.org/10.1016/0009-2614(96)00440-X.

[42] D.A. Thadathil, S. Varghese, K.B. Akshaya, R. Thomas, A. Varghese, An insight into photophysical investigation of (E)-2-Fluoro-N'-(1-(4-Nitrophenyl)Ethylidene) Benzohydrazide through solvatochromism approaches and computational studies, J. Fluoresc. 29 (2019) 1013–1027, https://doi.org/10.1007/s10895-019-02415-y.

[43] F. Trani, G. Scalmani, G. Zheng, I. Carnimeo, M.J. Frisch, V. Barone, Time-dependent density functional tight binding: new formulation and benchmark of excited states, J. Chem. Theory Comput. 7 (2011) 3304–3313, https://doi.org/10.1021/ct200461y.

[44] S. Beegum, Y.S. Mary, Y.S. Mary, R. Thomas, S. Armaković, S.J. Armaković, J. Zitko, M. Dolezal, C. Van Alsenoy, Exploring the detailed spectroscopic characteristics, chemical and biological activity of two cyanopyrazine-2-carboxamide derivatives using experimental and theoretical tools, Spectrochim. Acta - Part A Mol. Biomol. Spectrosc. 224 (2020) 1–13, https://doi.org/10.1016/j.saa.2019.117414.

[45] M. Petersilka, U.J. Gossmann, E.K.U. Gross, Excitation energies from time-dependent density-functional theory, Phys. Rev. Lett. 76 (1996) 1212–1215, https://doi.org/10.1103/PhysRevLett.76.1212.

[46] E. Runge, E.K.U. Gross, Density-functional theory for time-dependent systems, Phys. Rev. Lett. 52 (1984) 997–1000, https://doi.org/10.1103/PhysRevLett.52.997.

[47] Y. Sheena Mary, T. Ertan-Bolelli, R. Thomas, A.R. Krishnan, K. Bolelli, E.N. Kasap, T. Onkol, I. Yildiz, Quantum mechanical studies of three aromatic halogen-substituted bioactive sulfonamidobenzoxazole compounds with potential light harvesting properties, Polycycl. Aromat. Compd. In Press (2019)https://doi.org/10.1080/10406638.2019.1689405.

[48] A. Klamt, C. Moya, J. Palomar, A comprehensive comparison of the IEFPCM and SS(V)PE continuum solvation methods with the COSMO approach, J. Chem. Theory Comput. 11 (2015) 4220–4225, https://doi.org/10.1021/acs.jctc.5b00601.

[49] M. Hossain, R. Thomas, Y.S. Mary, K.S. Resmi, S. Armaković, S.J. Armaković, A.K. Nanda, G. Vijayakumar, C. Van Alsenoy, Understanding reactivity of two newly synthetized imidazole derivatives by spectroscopic characterization and computational study, J. Mol. Struct. 1158 (2018) 176–196, https://doi.org/10.1016/j.molstruc.2018.01.029.

[50] P. Kavitha Rani, Y. Sheena Mary, A. Fernandez, Y.S. Mary, R. Thomas, Single crystal XRD, DFT investigations and molecular docking study of 2-((1, 5-dimethyl-3-oxo-2-phenyl-2, 3-dihydro-1H-pyrazol-4-yl) amino) naphthalene-1, 4-dione as a potential anti-cancer lead molecule, Comput. Biol. Chem. 78 (2019) 153–164.

[51] Y.S. Mary, Y.S. Mary, R. Thomas, B. Narayana, S. Samshuddin, B.K. Sarojini, S. Armaković, S.J. Armaković, G.G. Pillai, Theoretical studies on the structure and various physico-chemical and biological properties of a terphenyl derivative with

immense anti-protozoan activity, Polycycl. Aromat. Compd. (2019) https://doi.org/10.1080/10406638.2019.1624974 In Press.
[52] R. Thomas, Y.S. Mary, K.S. Resmi, B. Narayana, B.K. Sarojini, G. Vijayakumar, C. Van Alsenoy, Two neoteric pyrazole compounds as potential anti-cancer agents: synthesis, electronic structure, physico-chemical properties and docking analysis, J. Mol. Struct. 1181 (2019) 455–466.
[53] S. Jeeva, S. Muthu, R. Thomas, B.R. Raajaraman, G. Mani, G. Vinitha, Co-crystals of urea and hexanedioic acid with third-order nonlinear properties: an experimental and theoretical enquiry, J. Mol. Struct. 1202 (2020) 127237, https://doi.org/10.1016/j.molstruc.2019.127237.
[54] J.S. Al-Otaibi, Y.S. Mary, S. Armaković, R. Thomas, Hybrid and bioactive cocrystals of pyrazinamide with hydroxybenzoic acids: detailed study of structure, spectroscopic characteristics, other potential applications and noncovalent interactions using SAPT, J. Mol. Struct. 1202 (2020) 127316, https://doi.org/10.1016/j.molstruc.2019.127316.
[55] Y.S. Mary, P.B. Miniyar, Y.S. Mary, K.S. Resmi, C.Y. Panicker, S. Armaković, S.J. Armaković, R. Thomas, B. Sureshkumar, Synthesis and spectroscopic study of three new oxadiazole derivatives with detailed computational evaluation of their reactivity and pharmaceutical potential, J. Mol. Struct. 1173 (2018) 469–480, https://doi.org/10.1016/j.molstruc.2018.07.026.
[56] R. Thomas, Y.S. Mary, K.S. Resmi, B. Narayana, S.B.K. Sarojini, S. Armaković, S.J. Armaković, G. Vijayakumar, C. Van Alsenoy, B.J. Mohan, Synthesis and spectroscopic study of two new pyrazole derivatives with detailed computational evaluation of their reactivity and pharmaceutical potential, J. Mol. Struct. 1181 (2019) 599–612, https://doi.org/10.1016/j.molstruc.2019.01.014.
[57] F. Weinhold, Natural bond orbital analysis: a critical overview of relationships to alternative bonding perspectives, J. Comput. Chem. 33 (2012) 2363–2379, https://doi.org/10.1002/jcc.23060.
[58] K. Haruna, V.S. Kumar, Y. Sheena Mary, S.A. Popoola, R. Thomas, M.S. Roxy, A.A. Al-Saadi, Conformational profile, vibrational assignments, NLO properties and molecular docking of biologically active herbicide1,1-dimethyl-3-phenylurea, Heliyon. 5 (2019), e01987, https://doi.org/10.1016/j.heliyon.2019.e01987.
[59] E. D. Glendening, A.E. Reed, J.E. Carpenter, F. Weinhold, NBO Version 3.1, (n.d.).
[60] P. Politzer, J.S. Murray, Molecular electrostatic potentials and chemical reactivity, Rev. Comput. Chem. (1991) 273–312, https://doi.org/10.1002/9780470125793.ch7.
[61] P. Politzer, J.S. Murray, The fundamental nature and role of the electrostatic potential in atoms and molecules, Theor. Chem. Accounts 108 (2002) 134–142, https://doi.org/10.1007/s00214-002-0363-9.
[62] Y.S. Mary, Y.S. Mary, K.S. Resmi, R. Thomas, DFT and molecular docking investigations of oxicam derivatives, Heliyon. 5 (2019), e02175, https://doi.org/10.1016/j.heliyon.2019.e02175.
[63] C.M. Breneman, M. Martinov, 3 - The Use of Electrostatic Potential Fields in QSAR and QSPR, K.B.T.-T in: J.S. Murray, C.C. Sen (Eds.), Mol. Electrost. Potentials, Elsevier 1996, pp. 143–179, https://doi.org/10.1016/S1380-7323(96)80043-4.
[64] M. Orozco, F.J. Luque, Generalization of the molecular electrostatic potential for the study of noncovalent interactions, K.B.T.-T in: J.S. Murray, C.C. Sen (Eds.), Mol. Electrost. Potentials, Elsevier 1996, pp. 181–218, https://doi.org/10.1016/S1380-7323(96)80044-6.
[65] P. Politzer, P. Lane, M.C. Concha, Atomic and molecular energies in terms of electrostatic potentials at nuclei, Int. J. Quantum Chem. 90 (2002) 459–463, https://doi.org/10.1002/qua.10105.
[66] C. Corminboeuf, T. Heine, G. Seifert, von R. Schleyer, J. Weber, Induced magnetic fields in aromatic [n]-annulenes—interpretation of NICS tensor components, Phys. Chem. Chem. Phys. 6 (2004) 273–276 https://doi.org/10.1039/B313383B.
[67] A. Stanger, NICS – past and present, Eur. J. Org. Chem. 2020 (2020) 3120–3127, https://doi.org/10.1002/ejoc.201901829.
[68] Z. Chen, C.S. Wannere, C. Corminboeuf, R. Puchta, Von R. Schleyer, Nucleus-independent chemical shifts (NICS) as an aromaticity criterion, Chem. Rev. 105 (2005) 3842–3888, https://doi.org/10.1021/cr030088.
[69] J.C. Dobrowolski, P.F.J. Lipiński, On splitting of the NICS(1) magnetic aromaticity index, RSC Adv. 6 (2016) 23900–23904, https://doi.org/10.1039/C6RA03246J.
[70] H. Fallah-Bagher-Shaidaei, C.S. Wannere, C. Corminboeuf, R. Puchta, P.V.R. Schleyer, Which NICS aromaticity index for planar π rings is best? Org. Lett. 8 (2006) 863–866, https://doi.org/10.1021/ol0529546.
[71] P. Politzer, J.S. Murray, F.A. Bulat, Average local ionization energy: a review, J. Mol. Model. 16 (2010) 1731–1742, https://doi.org/10.1007/s00894-010-0709-5.
[72] G.V. Gibbs, D.F. Cox, M.B. Boisen Jr., R.T. Downs, N.L. Ross, The electron localization function: a tool for locating favorable proton docking sites in the silica polymorphs, Phys. Chem. Miner. 30 (2003) 305–316, https://doi.org/10.1007/s00269-003-0318-2.
[73] F. Fuster, A. Sevin, B. Silvi, Topological analysis of the electron localization function (ELF) applied to the electrophilic aromatic substitution, J. Phys. Chem. A 104 (2000) 852–858, https://doi.org/10.1021/jp992783k.
[74] P. Fuentealba, E. Chamorro, J.C. Santos, Chapter 5 Understanding and using the electron localization function, in: A.B.T.-T, in: C.C. Toro-Labbé (Ed.), Theor. Asp. Chem. React, Elsevier 2007, pp. 57–85, https://doi.org/10.1016/S1380-7323(07)80006-9.
[75] V. Tsirelson, A. Stash, Analyzing experimental electron density with the localized-orbital locator, Acta Crystallogr. Sect. B. 58 (2002) 780–785, https://doi.org/10.1107/S0108768102012338.
[76] H.L. Schmider, A.D. Becke, Chemical content of the kinetic energy density, J. Mol. Struct. THEOCHEM 527 (2000) 51–61, https://doi.org/10.1016/S0166-1280(00)00477-2.
[77] H. Jacobsen, Localized-orbital locator (LOL) profiles of chemical bonding, Can. J. Chem. 86 (2008) 695–702, https://doi.org/10.1139/v08-052.
[78] X.-Y. Zhou, C. Rong, T. Lu, P. Zhou, S. Liu, Information functional theory: electronic properties as functionals of information for atoms and molecules, J. Phys. Chem. A 120 (2016) 3634–3642, https://doi.org/10.1021/acs.jpca.6b01197.
[79] J. Wu, D. Yu, S. Liu, C. Rong, A. Zhong, P.K. Chattaraj, S. Liu, Is it possible to determine oxidation states for atoms in molecules using density-based quantities? An information-theoretic approach and conceptual density functional theory study, J. Phys. Chem. A 123 (2019) 6751–6760, https://doi.org/10.1021/acs.jpca.9b05054.
[80] M. Alipour, Z. Badooei, Toward electron correlation and electronic properties from the perspective of information functional theory, J. Phys. Chem. A 122 (2018) 6424–6437, https://doi.org/10.1021/acs.jpca.8b05703.
[81] C. Rong, B. Wang, D. Zhao, S. Liu, Information-theoretic approach in density functional theory and its recent applications to chemical problems, WIREs Comput. Mol. Sci. 10 (2020), e1461, https://doi.org/10.1002/wcms.1461.
[82] Q. Wang, Y. Zhang, L. Wu, S. Niu, C. Song, Z. Zhang, G. Lu, C. Qiao, Y. Hu, K.Y. Yuen, Q. Wang, H. Zhou, J. Yan, J. Qi, Structural and functional basis of SARS-CoV-2 entry by using human ACE2, Cell. 181 (2020) https://doi.org/10.1016/j.cell.2020.03.045 894–904.e9.
[83] A.D. Mesecar, RCSB PDB - 6W63: Structure of COVID-19 Main Protease Bound to Potent Broad-Spectrum Non-covalent Inhibitor X77, RCSB, 2020 https://doi.org/10.2210/pdb6W63/pdb.
[84] Z. Jin, X. Du, Y. Xu, Y. Deng, M. Liu, Y. Zhao, B. Zhang, X. Li, L. Zhang, C. Peng, Y. Duan, J. Yu, L. Wang, K. Yang, F. Liu, R. Jiang, X. Yang, T. You, X. Liu, X. Yang, F. Bai, H. Liu, X. Liu, L.W. Guddat, W. Xu, G. Xiao, C. Qin, Z. Shi, H. Jiang, Z. Rao, H. Yang, Structure of Mpro from SARS-CoV-2 and discovery of its inhibitors, Nature. 582 (2020) 289–293, https://doi.org/10.1038/s41586-020-2223-y.
[85] J.S. Al-Otaibi, Y.S. Mary, R. Thomas, B. Narayana, Theoretical studies into the spectral characteristics, biological activity, and photovoltaic cell efficiency of four new polycyclic aromatic chalcones, Polycycl. Aromat. Compd. (2020) 1–15, https://doi.org/10.1080/10406638.2020.1747097.
[86] A. Bielenica, S. Beegum, Y.S. Mary, Y.S. Mary, R. Thomas, S. Armaković, S.J. Armaković, S. Madeddu, M. Struga, C. Van Alsenoy, Experimental and computational analysis of 1-(4-chloro-3-nitrophenyl)-3-(3, 4-dichlorophenyl) thiourea, J. Mol. Struct. 1205 (2020) 127587.
[87] J.S. Al-Otaibi, A.H. Almuqrin, Y.S. Mary, R. Thomas, Modeling the conformational preference, spectroscopic properties, UV light harvesting efficiency, biological receptor inhibitory ability and other physico-chemical properties of five imidazole derivatives using quantum mechanical and molecular mechanics t, J. Mol. Liq. 112871 (2020) https://doi.org/10.1016/j.molliq.2020.112871.
[88] Y.S. Priya, K.R. Rao, P.V. Chalapathi, A. Veeraiah, K.E. Srikanth, Y.S. Mary, R. Thomas, Intricate spectroscopic profiling, light harvesting studies and other quantum mechanical properties of 3-phenyl-5-isooxazolone using experimental and computational strategies, J. Mol. Struct. 1203 (2020) 127461, https://doi.org/10.1016/j.molstruc.2019.127461.
[89] V.S. Kumar, Y.S. Mary, K. Pradhan, D. Brahman, Y.S. Mary, R. Thomas, M.S. Roxy, C. Van Alsenoy, Synthesis, spectral properties, chemical descriptors and light harvesting studies of a new bioactive azo imidazole compound, J. Mol. Struct. 1199 (2020) 127035, https://doi.org/10.1016/j.molstruc.2019.127035.
[90] K. Haruna, V.S. Kumar, S.J. Armaković, S. Armaković, Y.S. Mary, R. Thomas, S.A. Popoola, A.R. Almohammedi, M.S. Roxy, A.A. Al-Saadi, Spectral characterization, thermochemical studies, periodic SAPT calculations and detailed quantum mechanical profiling various physico-chemical properties of 3, 4-dichlorodiuron, Spectrochim. Acta Part A Mol. Biomol. Spectrosc. 228 (2020) 117580.
[91] Y.S. Mary, G. Yalcin, Y.S. Mary, K.S. Resmi, R. Thomas, T. Önkol, E.N. Kasap, I. Yildiz, Spectroscopic, quantum mechanical studies, ligand protein interactions and photovoltaic efficiency modeling of some bioactive benzothiazolinone acetamide analogs, Chem. Pap. (2020) https://doi.org/10.1007/s11696-019-01047-7.
[92] K.E. Srikanth, A. Veeraiah, T. Pooventhiran, R. Thomas, K.A. Solomon, C.J.S. Raju, J.N.L. Latha, Detailed molecular structure (XRD), conformational search, spectroscopic characterization (IR, Raman, UV, fluorescence), quantum mechanical properties and bioactivity prediction of a pyrrole analogue, Heliyon. 6 (2020), e04106, .